



Early Activity in Comet C/2014 UN271 Bernardinelli–Bernstein as Observed by TESS

Tony L. Farnham¹, Michael S. P. Kelley¹, and James M. Bauer¹University of Maryland, Department of Astronomy, College Park, MD 20742, USA; farnham@astro.umd.edu

Received 2021 August 20; revised 2021 October 20; accepted 2021 October 20; published 2021 November 29

Abstract

We used long duration observations from the Transient Exoplanet Survey Satellite (TESS) to investigate the behavior of comet C/2014 UN271 Bernardinelli–Bernstein at large heliocentric distances. By combining data from sector 03 (976 30 minute exposures from 2018), and sectors 29 and 30 (3585 and 3410 10 minute exposures, respectively, from 2020), we produced deep coadded images of the comet. A comparison of these results with similarly processed images of inactive Kuiper Belt objects and asteroids reveals that the comet was already exhibiting coma at heliocentric distances 23.8 and 21.2 au, making this one of the most distant comets for which preperihelion activity has been directly detected. A simple syndyne analysis of asymmetries in the coma suggests that activity probably started several years prior to these observations, and likely arose from emission in roughly the sunward direction. The images were used to produce photometric lightcurves, though no rotational variability was detected. We used NEOWISE observations from 2020 November 26–28 to place an upper limit of 2×10^{28} molecules s^{-1} (3σ) on the CO production rate.

Unified Astronomy Thesaurus concepts: Comets (280); Comae (271); Long period comets (933); Oort cloud objects (1158)

1. Introduction

Comet C/2014 UN271 Bernardinelli–Bernstein (hereafter B-B) was first observed by the Dark Energy Survey (DES) at a heliocentric distance $r_h = 29.3$ au in 2014, with additional observations through 2018 (Bernstein & Bernardinelli 2021), but it was only discovered in 2021 when a focused trans-Neptunian object (TNO) search of the DES data was done (Bernardinelli et al. 2021b). Initial orbit integrations suggest that the comet came from the inner edge of the Oort cloud (Nakano 2021), though it may have entered the planetary region of the solar system before (Bernardinelli et al. 2021a). Early images appeared stellar, so it was assumed that there was no coma. Under this assumption, and with an absolute magnitude 7.8¹ and albedo ~ 0.1 , the size of the body was estimated to be >100 km in diameter, which would make it among the largest nuclei for known comets. Shortly after the announcement of its discovery in 2021, additional observations showed that B-B was exhibiting activity at $r_h = 20.2$ au (Buzzi & Veres 2021; Kokotanekova et al. 2021) and was indeed a comet.

The Transiting Exoplanet Survey Satellite (TESS) searches for extrasolar planets by observing a sector of the sky for ~ 27 days and using high-quality photometric measurements of the stars in the field to look for transits (Ricker et al. 2015). A TESS sector covers 84° of ecliptic longitude ($|l| > 6^\circ$) with four cameras, each with a 24° field of view (21 arcsec pixels). Images are obtained every 2 minutes and then coadded into either 30 minute exposures (for sectors 01–26) or 10 minute exposures (sectors 27+) that are saved as full-frame images (FFI). Because of the large field of view, solar system objects serendipitously appear in the images. We are taking advantage

of this phenomenon to conduct a study of the comets that have been observed in the survey (e.g., Farnham et al. 2019).

When the unique aspects of B-B came to light, we established that the comet had passed through the TESS field in 2018 and again in 2020. Its $V \sim 20$ magnitude means it is not a prime candidate for a full analysis of the temporal phenomena that we typically study in brighter comets, but the large number of observations allows us to coadd frames, producing deep images that can be used to look for coma. Thus, the TESS data allow us to investigate whether the comet might have been active earlier than previously thought.

2. Observations

B-B appeared in the sector 03 (camera 2, CCD #1) field for 27 days in 2018 and in the sector 29 (camera 3, CCD #1) and 30 (camera 3, CCD #2) fields spanning 76 days in 2020. Specific dates and their associated geometric conditions are listed in Table 1. During the first and last three days of the sector 03 observations, the spacecraft was testing new pointing software that increased the jitter and smear during these times (minimally in some images, significantly in others). Other suboptimal images in all three sectors include frames in which the comet passed near or over a star, and occasional frames that are smeared due to TESS momentum dumps that occur every ~ 2.5 days. We addressed these issues as described below.

3. Data Reduction and Analysis

3.1. Background Removal and Calibration

The wide-field FFI data are crowded with stars that must be removed to detect faint moving objects. We adopted the TESS user-provided Difference Image Analysis software (DIA; Oelkers & Stassun 2018) to perform this task. DIA is designed to identify objects whose brightnesses vary with time, and as an intermediate step in the reduction procedures the scattered light (from the Earth, Moon, etc.) and background stars are removed from each image. We use these intermediate, cleaned images, an

¹ Minor Planet Electronic Circular 2021-M53.



Original content from this work may be used under the terms of the [Creative Commons Attribution 4.0 licence](https://creativecommons.org/licenses/by/4.0/). Any further distribution of this work must maintain attribution to the author(s) and the title of the work, journal citation and DOI.

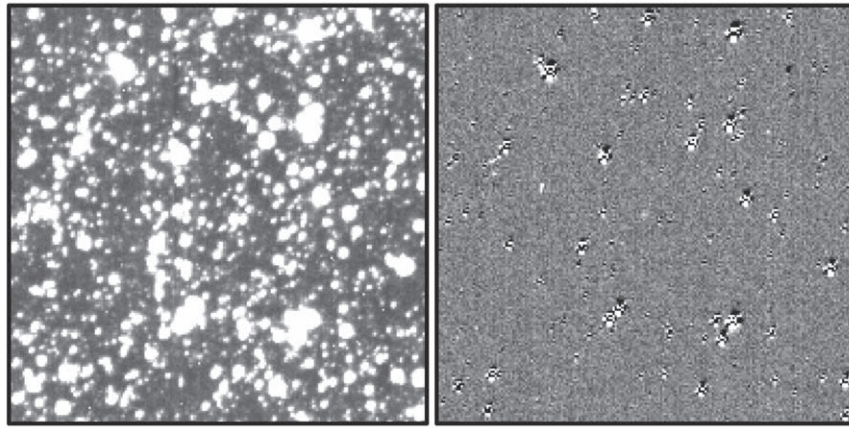


Figure 1. Example of the star and background removal, showing a $1^{\circ}1'$ region of a 10 minute frame from sector 30 (tess2020272035913-s0030-3-2-0195-s_ffic_sa). Panels show the image before (left) and after (right) the DIA cleaning process. B-B can be seen at the center of the cleaned frame.

Table 1
Geometric Conditions^a

Object	Dates ^b	r_h^c (au)	Δ^d (au)	α^e (deg.)	P.M. ^f (arcsec hr ⁻¹)	V (mag)	# Obs. ^g
Comparison Objects (2018)							
C/2014 UN271 B-B (S03)	2018 Sep 20-Oct 17	23.8	23.2	2.0	-4.9, -4.4	21.1	976 (30)
2010 TR19	2018 Sep 20-Oct 17	35.6	34.7	0.8	-3.2, -1.3	21.1	1090 (30)
2008 QY40	2018 Sep 20-Oct 17	36.9	36.0	0.4	-3.2, -1.0	21.2	1098 (30)
2010 RF64	2018 Sep 20-Oct 17	36.5	35.6	0.7	-3.0, -1.6	21.4	1010 (30)
2014 OZ61	2018 Sep 20-Oct 17	2.4	1.5	14.3	-27.6, -25.4	21.1	1063 (30)
Comparison Objects (2020)							
C/2014 UN271 B-B (S29)	2020 Aug 26-Sep 21	21.2	20.8	2.4	-3.3, -7.0	19.3	3585 (10)
C/2014 UN271 B-B (S30)	2020 Sep 23-Oct 20	21.1	20.7	2.4	-5.4, -4.9	19.3	3410 (10)
2001 UH132	2020 Sep 23-Oct 20	1.9	0.9	12.1	-37.2, 13.2	18.7	3423 (10)
443702	2020 Sep 23-Oct 20	2.1	1.1	12.2	-32.5, -6.1	19.7	3337 (10)
2015 VJ106	2020 Sep 23-Oct 20	2.3	1.3	11.7	-31.5, -4.3	19.6	3330 (10)
Weakly Active Comets							
66P/du Toit	2018 Sep 20-Oct 07	2.1	1.1	5.9	-50.5, 18.7	15.8	694 (30)
398P/Boattini	2020 Nov 20-Dec 16	1.3	0.4	24.7	14.1, 27.8	13.5	3493 (10)
371P/LINEAR-Skiff	2018 Sep 22-Oct 17	2.2	1.2	11.1	-27.3, 5.9	18.8	746 (30)
162P/Siding-Spring	2020 Jul 05-Jul 30	2.0	1.2	24.0	-2.4, -40.3	17.0	3350 (10)
C/2019 T4 ATLAS	2021 Jan 14-Feb 08	5.9	5.3	8.3	-13.8, 4.0	15.3	3066 (10)
C/2020 J1 SONEAR	2020 Jul 13-Jul 30	4.2	3.4	9.9	-64.8, -22.0	15.3	1990 (10)

Notes. Boldfaced entries highlight the comet of interest.

^a Geometric parameters at the midtime of the observation window.

^b Range of TESS observation dates.

^c Heliocentric distance.

^d Geocentric distance.

^e Solar phase angle.

^f Proper Motion, R.A. & decl. (arcsec hr⁻¹).

^g Number of observations in the coadded frame (parentheses denote 10 or 30 minute exposure times).

example of which is shown in Figure 1, for our comet analyses. The procedure does a good job removing the fainter stars and the wings of brighter stars, but due to the undersampled point-spread function (PSF; Vanderspek et al. 2018), uncorrelated residuals remain at the centers of bright stars. On occasion, these residuals can still interfere with the comet, but at a significantly lower level than the stars in the original images.

To minimize problems with bad images (streaked frames or those where star residuals interfere with the comet), we attempted to remove them from our analyses. In the course of its operations, the DIA routine measures the roundness and sharpness of stars in each image, and we used this information to

identify smeared frames. We computed the mean value of the parameters in surrounding frames, and rejected those frames that differ from the average by more than 5σ . Similarly, using an animated sequence of star-removed images, we manually identified frames in which the comet passed over residual background stars and removed those images from our analyses.

TESS pipeline products are calibrated to $e^- s^{-1}$, which can be converted to TESS magnitudes ($15,000 e^- s^{-1}$ corresponds to $T = 10.0$; Vanderspek et al. 2018). Using the Web TESS Viewing Tool², which requires an object's brightness in

² <https://heasarc.gsfc.nasa.gov/cgi-bin/tess/webtess/wtv.py>

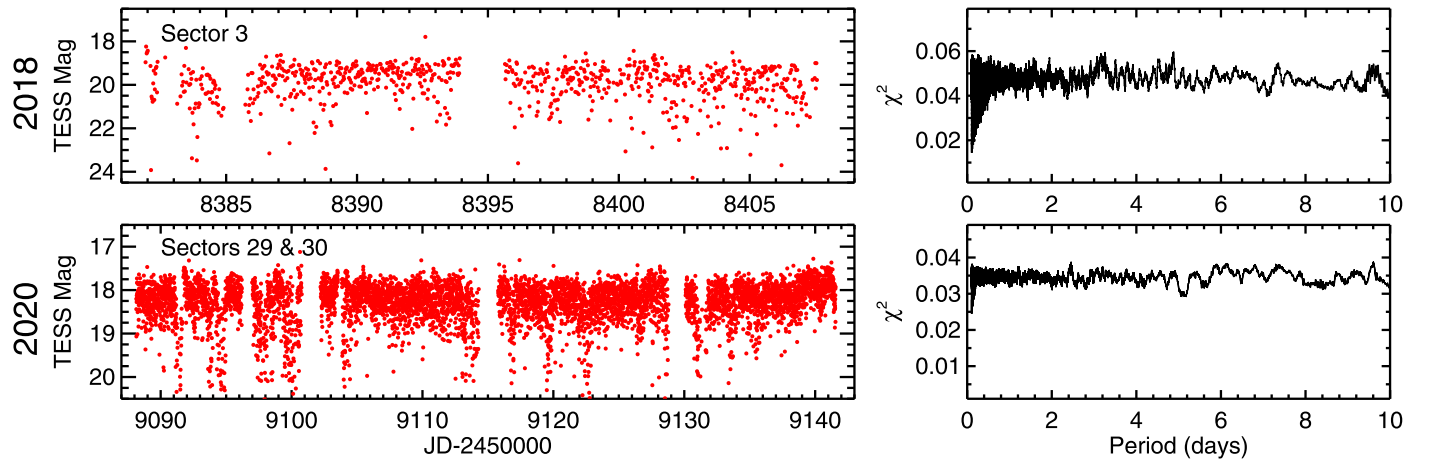


Figure 2. Left: lightcurves from the 2018 and 2020 sectors. Right: results from the PDM analysis for each lightcurve. In these plots, the baseline χ^2 level represents the dispersion of the randomly phased data, while a significant drop in χ^2 indicates a potential periodicity.

multiple spectral bandpasses, we derived rough conversions to V and R magnitudes. Using typical comet colors $V - J = 1.47 \pm 0.17$ and $J - H = 0.42 \pm 0.07$ (averages of 14 and 16 measurements, respectively, from seven Jupiter family comets (JFC) and one long-period comet (LPC); Hartmann et al. 1982) and $V - R = 0.5 \pm 0.03$ (average value from 63 JFCs, LPCs, and Active Centaurs (compiled by Jewitt 2015)), we find $V = T + 0.8$ and $R = T + 0.3$. The systematic uncertainties in converting from TESS magnitudes to V and R are dominated by the uncertainties in the comet colors, with conservative estimates of ± 0.3 mag in each case.

3.2. Photometric Lightcurve Analysis

Even though B-B is faint, we used its lightcurve to search for periodicity that might provide a constraint on its rotation state. We measured photometry of the comet using a 2.5 pixel radius aperture, and removed the sky background using the modal value in an annulus with radii of 5 and 15 pixels. The resulting lightcurves are shown in Figure 2. Because the signal from B-B is low in individual images, the photometry is affected by even small errors in the sky measurement. Thus, imperfect removal of structure in the sky background or star residuals in the annulus can have a notable effect on the lightcurve. This effect will be most pronounced when the measured sky level is too high, resulting in the larger deviations on the faint side of the lightcurve.

We used both a phase dispersion minimization routine (PDM; Stellingwerf 1978) and a Lomb-Scargle routine to look for periodicities in the lightcurves, evaluating periods from 0.1 to 10 days, with the results from the PDM analysis shown in Figure 2. The PDM-related χ^2 statistic in this plot is a measure of the amount of scatter in bins of data at different rotational phases. In principle, the χ^2 value will drop from the baseline for periods where the variations in the lightcurve align and reduce the scatter. As seen in the plots, there is no significant periodicity in either group of TESS data. (Note that the low χ^2 for periods < 1 day are spurious artifacts produced by clustering of data points in phase space at periods that alias the sampling cadence. This clustering produces artificially low measures of the dispersion that do not reflect valid periodicities.) Analyses from the Lomb-Scargle technique produced similar negative results, which is consistent with those of Ridden-Harper et al. (2021). We also looked at longer periods, experimented with

binning the measurements to increase the signal to noise, and explored different subsets of the data in case the nucleus' rotation rate was changing throughout the observations (e.g., variations may be masked when the data are phased to a constant period). As with the full data set, none of these tests revealed any significant periodicities.

These results allow us to rule out variability in the comet's lightcurve larger than the photometric uncertainties due to photon noise and sky background measurements (~ 0.3 mag), but at this time we cannot rule out variations below this level. Although the coma could be damping variability produced by rotation of the nucleus, this is not likely. Comparison of our data and those from other telescopes suggests that the coma is extensive but tenuous, allowing coadded TESS images, with large pixels, to resolve it while telescopes with higher spatial resolution may not. Thus, the coma is probably not affecting the nucleus size or any conclusions regarding its rotational state. (We note that Bernardinelli et al. 2021a find hints that the lightcurve may exhibit variations of ~ 0.2 mag.) These lightcurve results suggest that the nucleus is either not highly elongated, or else it is currently oriented such that its rotation axis is pointed generally toward the Sun.

3.3. Cometary Coma

We took advantage of the large volume of TESS data and coadded to produce deep images that we could use to investigate any faint coma. After removing the stars as described in Section 3.1, we registered the comet from each sector to a common position using ephemeris coordinates from Horizons³ and the images' World Coordinate System. We then combined images from each sector using a median filter to coadd the comet signal while removing the residuals of the background stars. We produced coadds of ~ 5 day groups of images as well as a very deep, full-sector coadd of all images. Even though sectors 29 and 30 are adjacent in time, we produced separate coadds for each, because the spacecraft roll angle differs by $\sim 23^\circ$ between them and we wanted to avoid any potential smearing that might arise from rotating the frames. Having two separate consecutive sectors also provides a consistency check on the reproducibility of any results that are found.

³ <https://ssd.jpl.nasa.gov/horizons.cgi>

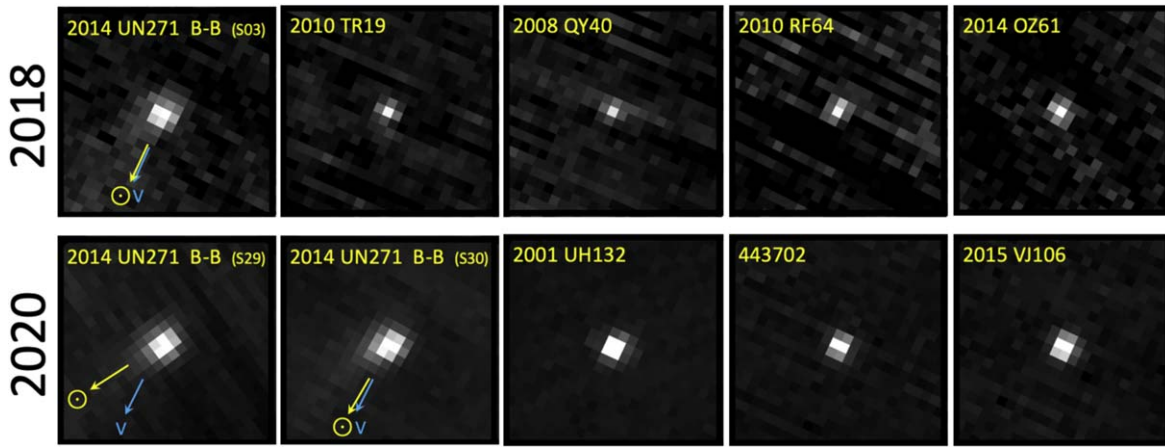


Figure 3. Coadded images of comet B-B (C/2014 UN271) from 2018 and 2020, showing coma with a sunward asymmetry. Coadded images from several Kuiper Belt objects and asteroids show examples of moving objects of similar brightness that are known to have no coma. The number of images combined in each coadd are listed in the last column of Table 1. Images shown here have been rotated in their entirety to place North up and East to the left, while preserving the coadded pixels. The median sunward direction for the sector is indicated. Each panel has a field of view of $8''.05$, which, for comet B-B, translates to 8.1×10^6 km in 2018 and 7.4×10^6 km in 2020.

The resulting full-sector coadded images are shown in Figure 3 and reveal that, in all three sectors, comet B-B exhibited a faint coma with an asymmetry in the sunward direction. This asymmetry is consistently visible in the individual 5 day coadds as well as in the full-sector coadds. Furthermore, the alignment of the asymmetry with respect to the sunward direction matches in both the sector 29 and 30 images, even with the 23° difference in roll angle, indicating that the asymmetry is independent of the orientation of the CCD pixels.

We were concerned that trailing of the comet during an exposure or the manipulation of the images while coadding the data might have artificially produced the appearance of a coma. To test these possibilities, we selected several inactive Kuiper Belt objects (KBOs) and asteroids of similar brightness that appear in the same sectors as B-B to use as comparison objects, and applied the same reduction procedures to produce coadds of those data. It was difficult to match the proper motions (KBOs tend to move slower and asteroids tend to move faster than B-B), but we chose objects that trailed <0.2 pixels during an exposure. The one exception to this was 2014 OZ61, which trailed by almost 1 pixel, and was included to evaluate how much of an effect an extreme amount of trailing would produce. The objects, along with their relevant geometric parameters are listed in Table 1 and the coadded images that were produced are shown in Figure 3 in all cases, the inactive objects are more centrally condensed than the comet.

To produce a quantitative comparison of the comet and the inactive objects, we took the full-sector coadded image for each object and plotted the pixel value against its cometocentric radius. We then fit a Gaussian profile to those points and measured its FWHM. The profiles, normalized so that the Gaussian peaks at 1.0, are shown in Figure 4. Even with the manipulation involved in coadding, the inactive objects are fairly consistent, with each having a FWHM between 1.8 and 2 pixels. This is consistent with measurements of the TESS point-spread function of typically 1–2 pixels, depending on stellar brightness and position on the image (Stassun et al. 2018). The FWHM of 2014 OZ61 is also in this range, indicating that even more extreme proper motions do not produce the appearance of a coma in an inactive body’s profile.

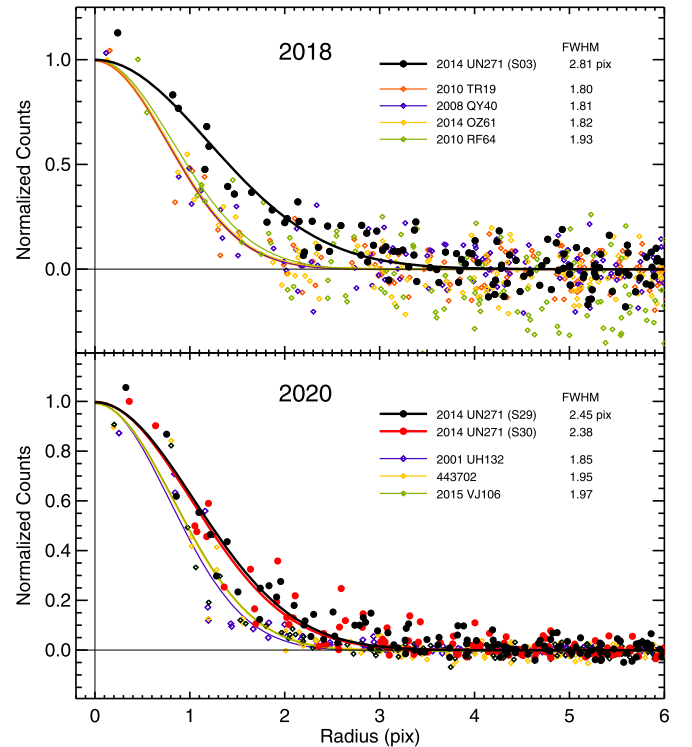


Figure 4. Radial profiles of comet B-B for 2018 and the two sectors from 2020, compared with KBOs and asteroids from the same times. The profiles for the comet are consistently broader than those for the inactive objects, which are all in the typical range of the TESS PSF. All curves have been normalized to 1 for comparison.

In all three sectors, the FWHM of comet B-B is notably broader than those of the comparison objects and are outside the typical range of the TESS PSF. Furthermore, the B-B profiles for the two 2020 sectors are very close, providing confidence that the measurements are robust. From these tests, it appears that neither proper motion nor the coadding process artificially introduces the appearance of a coma, supporting the argument that the coma around B-B is a real entity.

Our final test was to explore what coma in faint comets looks like in the TESS images. We selected six comets from our

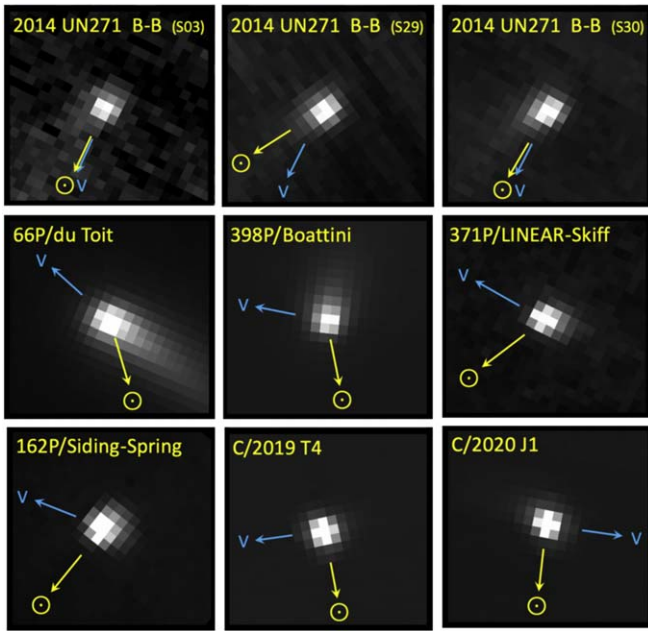


Figure 5. Coadded images of comet B-B compared with coadds of other faint comets that exhibit coma. The number of images combined in each coadd are listed in the last column of Table 1. North is up and east is to the left. Each panel has a field of view of 8.05 arcmin, which translates to as small a field as 1.4×10^5 km for 398P and fields of 8.1×10^6 km for comet B-B in 2018 and 7.4×10^6 km in 2020.

survey that are faint, but known to be active from other observations, or assumed to be active due to anomalous magnitudes. Some of these objects are inherently weak, while others have significant activity, but are faint because they are at larger geocentric distances. The geometric conditions are listed in Table 1. Comet 66P/du Toit, with a proper motion of 1.3 pixels per exposure, may suffer from some trailing, but the other objects all have trailing < 0.6 pixels, well within the level shown to be benign in our tests. We processed the comparison comet observations using the same techniques used for comet B-B.

The full-sector coadded images are shown in Figure 5 and the radial profiles are shown in Figure 6. Each of the six comets exhibits coma, as compared with the inactive objects above, though at differing levels. Similarly, the radial profiles of the comet have a range of FWHM, bracketing the width of the B-B profile. It is difficult to compare the details between these objects because of the wide range of brightness levels ($13.5 < V < 21.1$) and spatial scales (6000 to 353,000 km pix^{-1}), but these results, in conjunction with the KBO and asteroid tests above, show that the TESS observations are suitable for distinguishing between active comets and inactive bodies.

4. Discussion

4.1. Syndyne Analysis

The existence of the coma in comet B-B at a heliocentric distance of nearly 24 au raises the question “When did this object first become active?” We attempted to address this question by using syndynes and synchrones to explore the motions of the dust under the effects of gravity and radiation pressure. The syndynes associated with an observation show the locus of positions attained by a continuous emission of

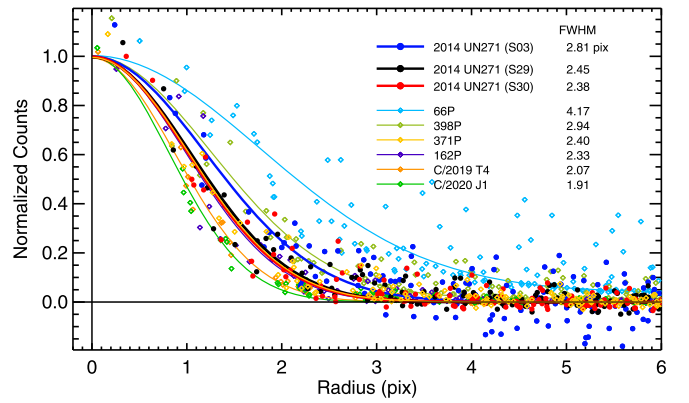


Figure 6. Comparison of the radial profiles from comet B-B to those from other active comets, which span a wide range of brightnesses and heliocentric distances. All curves have been normalized to 1.0 for comparison.

particles of a given size under the influence of radiation pressure. (This locus can be modified by including an emission velocity in a particular direction.) Due to diffusion of the dust after it is emitted, the syndyne represents the center of any feature that would be formed by those particles, giving a crude indication of where the material would be observed. Associated synchrones define where the particles emitted at a particular time would be located. These tools allow a simple means of investigating the general properties of a dust tail. For our three coadded images, plots of the syndynes (Finson & Probstein 1968) for dust emitted up to 10 yr before the date of observation are shown in Figure 7 along with images at the same orientation and scale. The first column of plots (labeled “0 m/s”) shows the standard syndynes for particle motions exclusively under the influence of radiation pressure. TESS’ viewpoint is close to the comet’s orbital plane, so these syndynes are clustered, overlapping in the anti-sunward direction. However, because all of the syndynes extend to the northwest, it is clear that the coma extension to the southeast is not comprised of grains exclusively under the influence of solar radiation pressure.

We then plotted the syndynes for grains emitted in the sunward direction with emission velocities 3.3, 10 and 33 m s^{-1} . Again these curves lie in the orbital plane, but some of the grains can travel to substantial distances from the nucleus in the sunward direction before they are turned back into the tail. Unfortunately, the overlap in the syndynes precludes a unique solution, but we can find combinations of particle sizes and emission velocities that allow a sunward extension of the coma to distances matching those in B-B (~ 100 arcsec). For example, the 0.5 mm syndyne, with emission velocities of 10 m s^{-1} produces an extension to nearly 100 arcsec, which would suggest that B-B would have been active for at least a decade prior to these observations. Alternatively, if the particles are emitted at 33 m s^{-1} , then a coma of 50 μm particles would extend to a distance of 100'' if the activity began around 2012.

Although the distances indicated by these tests are consistent, the position angle predicted by the syndynes ($\sim 150^\circ$) differs somewhat from the observed PA $\sim 125^\circ$. This is likely due to the comet having a more directed emission: either an isolated active area near the pole that is projected onto the sky at PA $\sim 125^\circ$, or else a small thermal lag that allows rotation to shift the emission enough to offset it from the syndynes. In either case, the shift in emission from the sunward direction need not be very large, because the solar phase angle

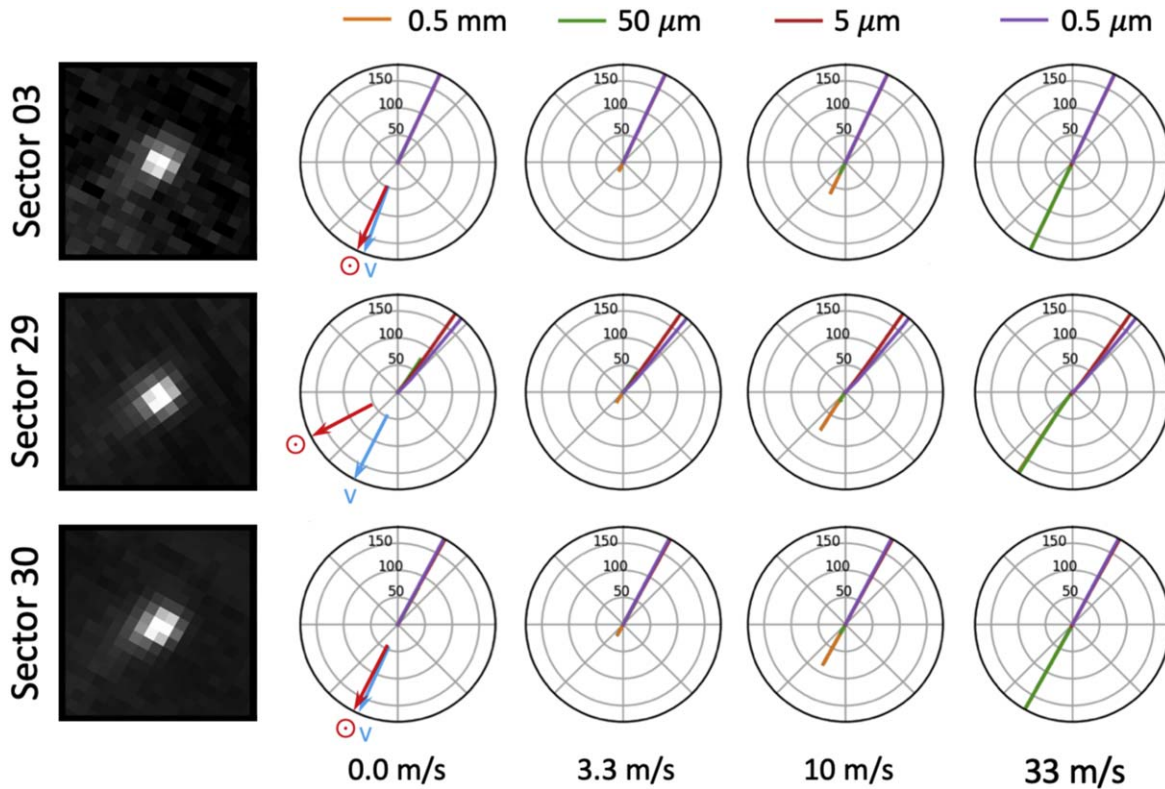


Figure 7. Comparison of the coadded images of comet B-B and plots of 10-year syndynes for grains of different radii (color bars at the top). The first column of syndynes shows motions for grains under the influence of radiation pressure alone, while subsequent columns show the motions for grains emitted in the sunward direction with velocities listed at the bottom. North is up and east is to the left. The images and plots are shown at the same scale, with radial distances in arcsec labeled in the plots. The sunward direction and velocity vector are given in the first syndyne plot so as to not obscure the sunward coma asymmetry in the images.

is $< 2^\circ.5$. With this level of projection, even a small deviation can produce a large shift when projected onto the sky (e.g., the sunward direction changes by 28° between sectors 29 and 30, even though the Earth-comet-Sun geometry changed little during this time.)

Even if the syndynes are not exact, the general motions of the grains, and thus their sizes and velocities, are still valid for the simple tests under consideration here. If we assume that the coma asymmetry is in the plane of the sky, then a projection of 100 arcsec in 2018 suggests dust has traveled at least 1.7×10^6 km from the nucleus. With an assumed velocity of 33 m s^{-1} , this indicates that the comet must have been active for at least 2 years. On the other hand, if there are any significant projection effects in the dust trajectories, then the distances increase proportionally, pushing the onset of activity to earlier times. At large heliocentric distances, emission is likely to be in the general direction of the Sun, introducing projection effects that would suggest the comet was probably active well before the comet was first observed in 2014.

There is a chance that the coma was the result of an outburst rather than continuous activity; however, B-B's long-term behavior would argue against it. If the coma was the result of an impulsive event, it should dissipate with time. However, the observed coma maintains the same appearance between the 2018 and 2020 observations, and if anything, becomes more centrally condensed over time. Also, the detection of activity in June 2021, after the announcement of the comet's discovery, confirms that the nucleus was active at 20.2 au, making it more likely that we are seeing continuous activity than a series of fortuitous outbursts. We note that outbursts observed after the discovery announcement Kelley et al. (2021) suggest that these

events could play a role in the onset of activity and warrant further monitoring and investigation.

4.2. Distant Comet Activity

Theoretical studies have suggested that long period and dynamically new comets could become active at extreme heliocentric distances (e.g., Meech & Svoren 2004, and references therein). However, only in the past decade or so have observations started to provide evidence to confirm these conjectures. For example, Meech et al. (2009) highlighted a number of comets that exhibited preperihelion activity, even though their perihelion distances were as large as 11.5 au, and when Comet C/2013 A1 Siding Spring had a close encounter to Mars in 2014, submillimeter sized dust, likely emitted from beyond 10 au, impacted the planet's atmosphere (Kelley et al. 2014; Tricarico et al. 2014; Ye & Hui 2014; Tricarico 2015).

With the increase in the discovery rate of faint comets, the heliocentric distance at which they are being found has also increased. Comet C/2010 U3 Boattini was observed to be active (in predisccovery observations from 2005) at 25.8 au (Hui et al. 2019), making it the most distant comet for which preperihelion activity has been directly observed. Similarly, predisccovery observations of comet C/2017 K2 PanSTARRS indicate that it was already active in 2013 (Hui et al. 2018), at a distance of 23.7 au, but studies of the development and evolution of its coma suggest it could have been active from as early as 35 au (Jewitt et al. 2021). The detection of coma in comet B-B at 23.8 au, with evidence that suggests it may have been active much earlier, makes it the third object known to be active at these extreme distances inbound.

It is interesting to compare comet B-B and C/2017 K2 PanSTARRS in light of their similarities. Coma was detected at ~ 24 au in both cases, with evidence suggesting that they were likely active for years before those measurements. The evidence indicates that the comae in both cases are comprised of submillimeter sized particles, emitted at low velocities. In their analysis of C/2017 K2, Jewitt et al. (2021) used the gas drag forces to derive a relationship between the grain size, a (mm), nucleus radius, r_N (km), heliocentric distance, r_H (au), and velocity, v (m sec^{-1}). Using this relation, $v = 23(r_N/a)^{1/2}/r_H$, with a 100 km nucleus at 24 au, we find the velocity of 0.1 to 0.5 mm grains to be ~ 10 to 21 m s^{-1} , which is perfectly consistent with the results we find from our syndyne analysis.

4.3. Volatile Sublimation

At these distances, water sublimation and amorphous ice crystallization both act too slowly to explain the activity producing the coma (Meech & Svoren 2004; Jewitt 2009). Several studies suggested that the activity in C/2017 K2 PanSTARRS was driven by CO sublimation (Yang et al. 2021; Meech et al. 2017), and it is likely that this is the species driving the activity in comet B-B. We used the NEOWISE reactivated mission data (Mainzer et al. 2014) in the public archive (Cutri et al. 2021) to investigate this possibility. NEOWISE observations taken 2020 November 26–28 (only 37 days after the sector 30 data), were stacked and analyzed using the techniques described in Bauer et al. (2021) and Bauer et al. (2015). In this analysis, we fit a solar spectrum through the $3.4 \mu\text{m}$ measurement to represent sunlight reflected from the dust continuum. We then compare the $4.6 \mu\text{m}$ band and assume that any excess in flux above the reflected light at that wavelength is signal from CO, which has an emission band in the $4.6 \mu\text{m}$ bandpass. (CO_2 also has emission in the bandpass, but we do not expect it to be significant because, at $r = 21$ au, its sublimation rate is many orders of magnitude lower than that of CO, as shown in the sublimation tool produced by Mike A’Hearn⁴, which uses the methods of Cowan & A’Hearn 1979). Unfortunately, neither bandpass showed any signal from the comet, even when we stacked and coadded 22 exposures, registered on the comet’s position. A CO production rate upper limit of 2×10^{28} molecules s^{-1} (3σ) was found for the signal within a 22 arcsec aperture centered on the comet’s predicted location, when B-B’s heliocentric distance was 20.92 au. To evaluate whether our derived upper limit on the CO production is sufficient to produce the observed coma, we compare it to measurements of comet Hale–Bopp (H-B), a highly active object with a large nucleus, whose CO production was characterized over a large range of heliocentric distance. Wierzbos et al. (2017) found the CO production for H-B, as a function of heliocentric distance, r , and scaled to the nucleus diameter, D , to be $Q(\text{CO})/D^2 = 3.5 \times 10^{29} D^{-2} r^{-2}$. For H-B’s diameter of 60 km and distance $r = 21$ au, H-B would have a scaled production rate $Q(\text{CO})_{\text{HB}}/D_{\text{HB}}^2 = 2.2 \times 10^{23}$ molecules $\text{s}^{-1} \text{ km}^{-2}$. Using our derived upper limit on CO production at 21 au and adopting a diameter $D_{\text{BB}} = 100$ km, we find $Q(\text{CO})_{\text{BB}}/D_{\text{BB}}^2 \leq 2 \times 10^{24}$ molecules $\text{s}^{-1} \text{ km}^{-2}$. Given that B-B’s upper limit is almost an order of magnitude higher than H-B’s computed production at the same distance, this suggests that CO is a viable candidate for generating the observed activity.

5. Conclusions

We used TESS observations of comet 2014 UN271 Bernardinelli–Bernstein (B-B) from 2018 and 2020 to investigate the early behavior of this comet at large heliocentric distances. The analyses include generating lightcurves for exploring rotational variability and using deep coadds of the images to evaluate the presence of coma (in comet B-B as well as in comparison objects) during these times. Results of our analyses are summarized here.

1. We have shown that coadding the extended duration TESS observations of solar system objects is an effective technique that can be used to detect faint coma and to differentiate between active and inactive objects.
2. The observations show that B-B exhibited a coma in both 2018 and 2020, when the comet was at heliocentric distances of 23.8 and 21.2 au. These detections, plus observations of coma from other observers in 2021 suggest that the activity is continuous, as opposed to the result of sporadic outbursts.
3. A simple syndyne analysis of the coma suggests that it is composed of submillimeter sized grains emitted at speeds of tens of m s^{-1} in the sunward direction. The activity likely started at least two years before the TESS observations and possibly as early as a decade before.
4. NEOWISE observations of B-B from November 2020 were used to put an upper limit of 2×10^{28} molecules s^{-1} (3σ) on the CO production rates.
5. Lightcurves from the two TESS epochs show no periodic variability, at least to within the uncertainties of the photometry (~ 0.3 mag). This result could put limits on the elongation of the nucleus or the orientation of the spin axis.

This paper includes data collected by the TESS mission, which are publicly available from the Mikulski Archive for Space Telescopes (MAST). Funding for the TESS mission is provided by NASA’s Science Mission directorate. This publication makes use of data products from the Near-Earth Object Wide-field Infrared Survey Explorer (NEOWISE), which is a joint project of the Jet Propulsion Laboratory/California Institute of Technology and the University of Arizona. NEOWISE is funded by the National Aeronautics and Space Administration. Support for this work was provided by the TESS Guest Observer program (80NSSC21K0337) and the NASA Solar System Workings Program (80NSSC21K0156).

Facilities: TESS, NEOWISE.

Software: DIA (Oelkers et al. 2015; Oelkers & Stassun 2018),

ORCID iDs

Tony L. Farnham  <https://orcid.org/0000-0002-4767-9861>

Michael S. P. Kelley  <https://orcid.org/0000-0002-6702-7676>

James M. Bauer  <https://orcid.org/0000-0001-9542-0953>

References

- Bauer, J. M., Gicquel, A., Kramer, E., & Meech, K. J. 2021, *PSJ*, 2, 34
 Bauer, J. M., Stevenson, R., Kramer, E., et al. 2015, *ApJ*, 814, 85
 Bernardinelli, P. H., Bernstein, G. M., Montet, B. T., et al. 2021a, arXiv:2109.09852

⁴ <https://pdssbn.astro.umd.edu/tools/ma-evap/index.shtml>

- Bernardinelli, P. H., Bernstein, G. M., Sako, M., et al. 2021b, arXiv:2109.03758
- Bernstein, P., & Bernardinelli, G. 2021, CBET, 4389, 1
- Buzzi, L., & Veres, P. 2021, CBET, 4989, 1
- Cowan, J. J., & A'Hearn, M. F. 1979, *M&P*, 21, 155
- Cutri, R. M., Mainzer, A., Conrow, T., et al. 2021, Explanatory Supplement to the NEOWISE Data Release Products, <https://wise2.ipac.caltech.edu/docs/release/neowise/expsup/index.html>
- Farnham, T. L., Kelley, M. S. P., Knight, M. M., & Feaga, L. M. 2019, *ApJL*, 886, L24
- Finson, M., & Probst, R. 1968, *ApJ*, 154, 327
- Hartmann, W. K., Cruikshank, D. P., & Degewij, J. 1982, *Icar*, 52, 377
- Hui, M.-T., Farnocchia, D., & Micheli, M. 2019, *AJ*, 157, 162
- Hui, M.-T., Jewitt, D., & Clark, D. 2018, *AJ*, 155, 25
- Jewitt, D. 2009, *AJ*, 137, 4296
- Jewitt, D. 2015, *AJ*, 150, 201
- Jewitt, D., Kim, Y., Mutchler, M., et al. 2021, *AJ*, 161, 188
- Kelley, M. S. P., Farnham, T. L., Bodewits, D., Tricarico, P., & Farnocchia, D. 2014, *ApJL*, 792, L16
- Kelley, M. S. P., Lister, T., & Holt, C. 2021, *ATel*, 14917, 1
- Kokotanekova, R., Lister, T., Bannister, M., et al. 2021, *ATel*, 14733, 1
- Mainzer, A., Bauer, J., Cutri, R. M., et al. 2014, *ApJ*, 792, 30
- Meech, K. J., Kleyna, J. T., Hainaut, O., et al. 2017, *ApJL*, 849, L8
- Meech, K. J., Pittichová, J., Bar-Nun, A., et al. 2009, *Icar*, 201, 719
- Meech, K. J., & Svoren, J. 2004, in *Comets II*, ed. M. C. Festou, H. U. Keller, & H. A. Weaver (Tucson, AZ: Univ. Arizona Press), 317
- Nakano, S. 2021, CBET, 4989, 1
- Oelkers, R. J., Macri, L. M., Wang, L., et al. 2015, *AJ*, 149, 50
- Oelkers, R. J., & Stassun, K. G. 2018, *AJ*, 156, 132
- Ricker, G. R., Winn, J. N., Vanderspek, R., et al. 2015, *JATIS*, 1, 014003
- Ridden-Harper, R., Bannister, M. T., & Kokotanekova, R. 2021, *RNAAS*, 5, 161
- Stassun, K. G., Oelkers, R. J., Pepper, J., et al. 2018, *AJ*, 156, 102
- Stellingwerf, R. 1978, *ApJ*, 224, 953
- Tricarico, P. 2015, *GeoRL*, 42, 4752
- Tricarico, P., Samarasinha, N. H., Sykes, M. V., et al. 2014, *ApJL*, 787, L35
- Vanderspek, R., Doty, J., Fausnaugh, M. M., et al. 2018, TESS Instrument Handbook, v0.1, Mikulski Archive for Space Telescopes, https://archive.stsci.edu/missions/tess/doc/TESS_Instrument_Handbook_v0.1.pdf
- Wierzchos, K., Womack, M., & Sarid, G. 2017, *AJ*, 153, 230
- Yang, B., Jewitt, D., Zhao, Y., et al. 2021, *ApJL*, 914, L17
- Ye, Q.-Z., & Hui, M.-T. 2014, *ApJ*, 787, 115